

Northumbria Research Link

Citation: McLaughlin, James, Thurgood, Jonathan, Botha, Gert and Wiggs, Joshua A. (2019) 3D WKB solution for fast magnetoacoustic wave behaviour within a separatrix dome containing a coronal null point. Monthly Notices of the Royal Astronomical Society, 484 (1). pp. 1390-1400. ISSN 0035-8711

Published by: Oxford University Press

URL: <https://doi.org/10.1093/mnras/stz085> <<https://doi.org/10.1093/mnras/stz085>>

This version was downloaded from Northumbria Research Link:
<http://nrl.northumbria.ac.uk/id/eprint/38204/>

Northumbria University has developed Northumbria Research Link (NRL) to enable users to access the University's research output. Copyright © and moral rights for items on NRL are retained by the individual author(s) and/or other copyright owners. Single copies of full items can be reproduced, displayed or performed, and given to third parties in any format or medium for personal research or study, educational, or not-for-profit purposes without prior permission or charge, provided the authors, title and full bibliographic details are given, as well as a hyperlink and/or URL to the original metadata page. The content must not be changed in any way. Full items must not be sold commercially in any format or medium without formal permission of the copyright holder. The full policy is available online: <http://nrl.northumbria.ac.uk/policies.html>

This document may differ from the final, published version of the research and has been made available online in accordance with publisher policies. To read and/or cite from the published version of the research, please visit the publisher's website (a subscription may be required.)



**Northumbria
University**
NEWCASTLE



UniversityLibrary

3D WKB solution for fast magnetoacoustic wave behaviour within a separatrix dome containing a coronal null point

James A. McLaughlin¹,¹★ Jonathan O. Thurgood^{1,2}, Gert J. J. Botha¹ and Joshua A. Wiggs^{1,3}

¹Department of Mathematics, Physics and Electrical Engineering, Northumbria University, Newcastle upon Tyne NE1 8ST, UK

²Division of Mathematics, University of Dundee, Dundee DD1 4HN, UK

³Department of Physics, Lancaster University, Lancaster LA1 4YB, UK

Accepted 2019 January 6. Received 2019 January 4; in original form 2018 October 10

ABSTRACT

The propagation of the fast magnetoacoustic wave is studied within a magnetic topology containing a 3D coronal null point whose fan field lines form a dome. The topology is constructed from a magnetic dipole embedded within a global uniform field. This study aims to improve the understanding of how magnetohydrodynamics (MHD) waves propagate through inhomogeneous media, specifically in a medium containing an isolated 3D magnetic null point. We consider the linearized MHD equations for an inhomogeneous, ideal, cold plasma. The equations are solved utilizing the WKB approximation and Charpit's Method. We find that for a planar fast wave generated below the null point, the resultant propagation is strongly dependent upon initial location and that there are two main behaviours: the majority of the wave escapes the null (experiencing different severities of refraction depending upon the interplay with the equilibrium Alfvén-speed profile) or, alternatively, part of the wave is captured by the coronal null point (for elements generated within a specific critical radius about the spine and on the $z = 0$ plane). We also generalize the magnetic topology and find that the height of the null determines the amount of wave that is captured. We conclude that for a wavefront generated below the null point, nulls at a greater height can trap proportionally less of the corresponding wave energy.

Key words: Magnetic fields – Waves – Sun: corona – (magnetohydrodynamics) MHD.

1 INTRODUCTION

The solar corona is replete with oscillations and wave behaviour, which is well described by magnetohydrodynamics (MHD; see e.g. Roberts 2004; De Moortel 2005; Nakariakov & Verwichte 2005), and various types of MHD waves have been observed by several solar instruments (see Nakariakov et al. 2016, for a recent review). From both theoretical considerations as well as observations, it is clear that the propagation, evolution, and behaviour of MHD waves is linked intimately with the magnetic topology of the region in which they manifest. Thus, in order to understand MHD wave behaviour in the solar corona, one must also understand the topology of the coronal magnetic field.

Potential field extrapolations of the coronal magnetic field can be made from magnetograms of the photosphere (e.g. see Régnier 2013) and these extrapolations show the topology (structure) of the magnetic field can contain two key features: *null points* – locations within a magnetic topology in which the field strength

is zero (see Longcope 2005; Régnier, Parnell & Haynes 2008; Priest 2014; Edwards & Parnell 2015), and *separatrix surfaces* – topological surfaces that separate regions of different magnetic flux connectivity. Null points occur naturally wherever there exist multiple flux fragments in a domain. By considering these fundamental elements of a field's configuration, one can prescribe the *magnetic skeleton* of the topology. Parnell et al. (1996) investigated and classified the different types of linear magnetic null points that can exist. Topologically, 3D null points consist of two key features: a special, isolated field line called the *spine*, which approaches (or recedes from) the null from above and below (Priest & Titov 1996) and a *fan* surface consisting of field lines spreading out from (or approaching) the null. Null points have received considerable attention as they are locations at which magnetic reconnection can occur (e.g. Priest & Forbes 2000; Pontin, Hornig & Priest 2005; McLaughlin et al. 2009). Null points occur not only within solar magnetic field configurations but can be found throughout nature, such as in the Earth's magnetic field (Finn 2006).

From potential field extrapolations and observations, it is evident that both MHD waves and magnetic null points are present throughout the solar corona. It is therefore natural to assume that MHD

* E-mail: james.a.mclaughlin@northumbria.ac.uk

waves will encounter these magnetic features. This paper follows a series of papers studying the interactions between MHD waves and various magnetic null point topologies (McLaughlin & Hood 2004, 2005, 2006a,b; McLaughlin, Ferguson & Hood 2008; Thurgood & McLaughlin 2012, 2013a,b; McLaughlin et al. 2016). This series of papers suggest that it is a generic result that fast mode waves will be attracted to the close vicinity of magnetic null points due to a refraction effect, where they subsequently concentrate energy on small scales, experiencing enhanced visco-resistive dissipation and triggering magnetic reconnection (the specific physics of which have been considered by Thurgood, Pontin & McLaughlin 2017, 2018a,b). Here, specifically, we consider the behaviour of the fast MHD wave in the neighbourhood of a coronal null point located at the apex of a separatrix dome, i.e. a 3D null whose field lines form a magnetic dome configuration. This configuration is more physically representative of the coronal magnetic field than previously considered. Crucially, we aim to assess the extent to which wavefronts emanating from below such a null (representing upwardly-propagating wave-energy flux from the solar surface) may be attracted to and trapped in the close vicinity of such a null.

The Wentzel–Kramers–Brillouin (WKB) approximation is a mathematical technique which utilizes an expansion approach to approximate exponential waveforms (see e.g. Bender & Orszag 1978; Tracey et al. 2014). For this technique to be applied the system must contain a large parameter. Since the typical spatial scales of the medium that fast waves propagate through is much larger than their typical wavelength, the WKB approximation provides an ideal tool for examining the propagation of the fast magnetoacoustic wave. Several authors have utilized the technique successfully in a solar context (e.g. Khomenko & Collados 2006 consider propagation in a magnetic sunspot-like structure; Afanasyev & Uralov 2011, 2012 consider aspects of solar shocks in a non-linear extension of the WKB method). However, the use of the WKB approximation is not just limited to astrophysical applications; the approximation is used in many other branches of physics, for example in quantum mechanics, where it can be used to calculate an approximate solution to Schrödinger’s equation (see Griffiths 2004). Within the wider topic of ray tracing methods, Núñez (2017, 2018) studied the geometry of rays and wavefronts associated with the fast magnetosonic wave and applied the results to the formation of shock waves and to current sheets. Of particular interest to this article is the work of McLaughlin et al. (2008) who utilized the WKB approximation to investigate MHD wave behaviour in the neighbourhood of a fully 3D null point. The authors utilized the technique to determine the transient properties of the fast and Alfvén modes in a linear, $\beta = 0$ plasma regime. However, McLaughlin et al. (2008) considered a simple 3D null point whose magnetic field strength becomes unphysically large as one moves far away from the null. In contrast, the magnetic field considered in this paper is more physically representative of the coronal magnetic field and removes this limitation (see Section 2.2).

The topology described in this paper exists above any parasitic polarity region and is a common feature in potential field extrapolations. Such a topology has been investigated by other authors: Pontin, Priest & Galsgaard (2013) considered a topology constructed from magnetic monopoles and investigated the properties of reconnection in such a system, and Tarr, Linton & Leake (2017) used three magnetic monopoles to construct a 2D magnetic dome topology (in 2D, these manifest as *separatrices* rather than *separatrix surfaces*), embedded within a model stratified solar atmosphere with the null at a coronal altitude. For a wave packet generated at the photosphere, Tarr et al. (2017) found that

the wave propagates into the 2D dome topology and that a portion of the wave refracts towards the null owing to the varying Alfvén speed, and that approximately 15.5 per cent of the wavepacket’s initial energy converges on the null. In contrast to the monopole approach, Candelaresi, Pontin & Hornig (2016) considered a dome topology constructed from analytical expressions for a dipole and uniform field. They considered the effects of photospheric footpoint motions as an input of energy into the topology. In this paper, we consider a similar analytical set-up to that of Candelaresi et al. (2016).

The paper has the following structure: the equations utilized to describe the system are detailed in Section 2, including assumptions, simplifications, linearization, and non-dimensionalization. This section will also outline the construction of the specific magnetic topology through which the fast wave will propagate (Section 2.2). Section 3 details the utilization of the WKB approximation and the isolation of the fast wave, and Section 4 presents the results obtained. Section 5 calculates the percentage of wave captured and the alterations this makes to the propagation of the fast wave. The conclusions are presented in Section 6. Appendix A details a generalization of the magnetic topology.

2 GOVERNING EQUATIONS

To study the propagation of MHD waves through a plasma it is first necessary to construct a mathematical model of the environment. This can be achieved by utilizing the following resistive, adiabatic MHD equations to describe an inhomogeneous plasma

$$\begin{aligned} \rho \frac{\partial \mathbf{v}}{\partial t} + \rho(\mathbf{v} \cdot \nabla) \mathbf{v} &= -\nabla p + \mathbf{j} \times \mathbf{B} + \rho \mathbf{g}, \\ \frac{\partial \mathbf{B}}{\partial t} &= \nabla \times (\mathbf{v} \times \mathbf{B}) + \eta \nabla^2 \mathbf{B}, \\ \frac{\partial \rho}{\partial t} + \nabla \cdot (\rho \mathbf{v}) &= 0, \\ \frac{\partial p}{\partial t} + \mathbf{v} \cdot \nabla p &= -\gamma p \nabla \cdot \mathbf{v}, \\ \mu \mathbf{j} &= \nabla \times \mathbf{B}, \end{aligned} \quad (1)$$

where ρ is the mass density, \mathbf{v} is the plasma velocity, t denotes time, p is the gas pressure, \mathbf{j} is electric current density, \mathbf{B} is magnetic induction (usually called the magnetic field), \mathbf{g} is gravitational acceleration, η is magnetic diffusivity, γ is the adiabatic index, and μ is the magnetic permeability.

2.1 Linearization and non-dimensionalization

We will utilize the linearized MHD equations in order to study wave propagation in our system. To do this, for each variable a , we assume $a = a_0 + \varepsilon a_1$, where a_0 is the equilibrium quantity, a_1 is the perturbed quantity, and ε is a small parameter such that $\varepsilon \ll 1$. Hence, equation (1) becomes

$$\rho_0 \frac{\partial \mathbf{v}_1}{\partial t} = -\nabla p_1 + \mathbf{j}_0 \times \mathbf{B}_1 + \mathbf{j}_1 \times \mathbf{B}_0 + \rho_1 \mathbf{g} \quad (2)$$

$$\frac{\partial \mathbf{B}_1}{\partial t} = \nabla \times (\mathbf{v}_1 \times \mathbf{B}_0) + \eta \nabla^2 \mathbf{B}_1, \quad (3)$$

$$\frac{\partial \rho_1}{\partial t} + \nabla \cdot (\rho_0 \mathbf{v}_1) = 0, \quad (4)$$

$$\frac{\partial p_1}{\partial t} + \mathbf{v}_1 \cdot \nabla p_0 = -\gamma p_0 \nabla \cdot \mathbf{v}_1, \quad (5)$$

$$\mu \mathbf{j}_1 = \nabla \times \mathbf{B}_1, \quad (6)$$

where we choose $\mathbf{v}_0 = 0$. We then consider the following simplifications: we choose a potential equilibrium magnetic field ($\nabla \times \mathbf{B}_0 = \mu \mathbf{j}_0 = 0$), as well as an ideal plasma ($\eta = 0$); gravitational effects are neglected ($\mathbf{g} = 0$); and the equilibrium density, ρ_0 , is assumed to be uniform¹. Given that, in the coronal plasma we are modelling, magnetic pressure dominates over gas pressure, i.e. $\beta \ll 1$, we consider a ‘cold’ plasma assumption². This is achieved via setting $p_0 = 0$.

The equations are now subjected to the following decompositions in order to render them dimensionless: we let $x = L\tilde{x}$, $y = L\tilde{y}$, $z = L\tilde{z}$, $\mathbf{v}_1 = v\tilde{\mathbf{v}}_1$, $\mathbf{B}_0 = B\tilde{\mathbf{B}}_0$, $\mathbf{B}_1 = B\tilde{\mathbf{B}}_1$, $t = T\tilde{t}$, and $\nabla = \tilde{\nabla}/L$, where \tilde{x} , \tilde{y} , \tilde{z} , $\tilde{\mathbf{v}}_1$, $\tilde{\mathbf{B}}_0$, $\tilde{\mathbf{B}}_1$, \tilde{t} , and $\tilde{\nabla}$ are the dimensionless quantities and L , v , B , T are constants of dimensionality for their respective variable. We then set v as a constant background Alfvén speed, namely $v = B/\sqrt{\mu\rho_0}$, as well as $v = L/T$. Under this non-dimensionalization, $\tilde{t} = 1$ refers to $t = T = L/v$, i.e. the Alfvén time taken to travel distance L .

For the rest of this paper, the tides are now dropped from the dimensionless quantities (that they are non-dimensionalized is understood) yielding the following non-dimensionalized, linearized equations for a cold, ideal plasma

$$\frac{\partial \mathbf{v}_1}{\partial t} = (\nabla \times \mathbf{B}_1) \times \mathbf{B}_0, \quad \text{and} \quad \frac{\partial \mathbf{B}_1}{\partial t} = \nabla \times (\mathbf{v}_1 \times \mathbf{B}_0),$$

which can be brought together in a single wave equation

$$\frac{\partial^2 \mathbf{v}_1}{\partial t^2} = \{\nabla \times [\nabla \times (\mathbf{v}_1 \times \mathbf{B}_0)]\} \times \mathbf{B}_0. \quad (7)$$

Hence, given a suitable choice for the equilibrium magnetic field, \mathbf{B}_0 , it is possible to obtain the perturbed velocity, \mathbf{v}_1 .

2.2 Magnetic topology

We wish to consider an isolated 3D null point located at the apex of a separatrix dome. Thus, we consider a similar analytical set-up to that of Candelaesi et al. (2016) namely we consider a Cartesian domain with a magnetic topology consisting of a (parasitic) magnetic dipole within a (global) uniform field. The topology is created by considering a vector potential, \mathbf{A} , such that $\mathbf{B} = \nabla \times \mathbf{A}$. The dipole field can be calculated by taking the dipole magnetic moment, $\mathbf{m} = (0, 0, -1)$, where the negative sign on \mathbf{m} ensures a parasitic polarity relative to the uniform field. Given position vector $\mathbf{r} = (x, y, z)$, the dipole is placed at $\mathbf{r}_0 = (0, 0, d)$. In this paper, we choose $d = -0.2$. This corresponds to a model ‘photosphere’ at $z = 0$, where the dipole is centred at $x = y = 0$ and buried at a depth of $|d|$. Following Shadowitz (1975), the (non-dimensionalized) equilibrium vector potential for the dipole is calculated via

$$\mathbf{A}_{\text{dipole}}(\mathbf{r}) = \frac{\mathbf{m} \times (\mathbf{r} - \mathbf{r}_0)}{|\mathbf{r} - \mathbf{r}_0|^3},$$

from which the dipole magnetic field is calculated: $\mathbf{B}_{\text{dipole}} = \nabla \times \mathbf{A}_{\text{dipole}}$. The full equilibrium magnetic topology in our system is

¹Note that spatial inhomogeneity in ρ_0 can lead to phase mixing, see e.g. Heyvaerts & Priest (1982); Nakariakov, Roberts & Murawski (1997); Botha et al. 2000; McLaughlin, De Moortel & Hood (2011a).

²Note that this is not strictly true for wave-null interactions since $\mathbf{B} \rightarrow 0$ at the null itself, but we note that the cold plasma assumption is a good approximation away from and near the null.

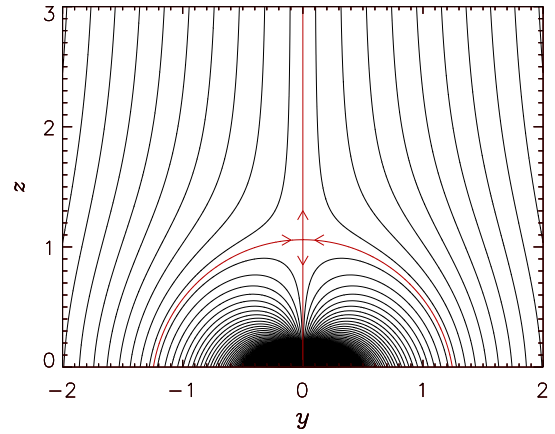


Figure 1. Rotationally-symmetric equilibrium magnetic field in the $x = 0$, yz -plane. Dipole is located at $x = y = 0$ and $z = d = -0.2$. 3D null point is located at $x = y = 0$, at a height $z = 2^{1/3} + d = 2^{1/3} - 0.2 = 1.05992$. Black lines denote magnetic field lines, and red lines indicate the magnetic skeleton in this plane: $y = 0$ denotes the *spine* and the curve denotes the *separatrix fan surface*: here $y^2 + (z - d)^2 = 2^{2/3}$. Arrows indicate the magnetic field direction.

created by adding a uniform magnetic field $\mathbf{B}_{\text{uniform}} = (0, 0, 1)$. This gives the equilibrium magnetic field which will be used throughout this paper,

$$\mathbf{B}_0 = \mathbf{B}_{\text{dipole}} + \mathbf{B}_{\text{uniform}} = (B_x, B_y, B_z),$$

where the individual components of the magnetic field can be expressed as follows:

$$\begin{aligned} B_x &= -\frac{3x(z-d)}{[x^2 + y^2 + (z-d)^2]^{5/2}}, \\ B_y &= -\frac{3y(z-d)}{[x^2 + y^2 + (z-d)^2]^{5/2}}, \\ B_z &= \frac{x^2 + y^2 - 2(z-d)^2}{[x^2 + y^2 + (z-d)^2]^{5/2}} + 1. \end{aligned} \quad (8)$$

This constructs a system with an isolated 3D null point which is located on $x = y = 0$ at height $z = 2^{1/3} + d = 2^{1/3} - 0.2 = 1.05992$ (the height of the null within the topology is calculated by setting $\mathbf{B}_0 = 0$). The separatrix surface of this null extends down to the $z = 0$, xy -plane forming a dome shape. The equilibrium magnetic field in the $x = 0$, yz -plane – $\mathbf{B}_0(0, y, z)$ – can be seen in Fig. 1, where magnetic field lines are indicated as black lines. Here, the red lines indicate the key topological features – the *magnetic skeleton* – which divides the connectivity of the region in this plane: the line $y = 0$ denotes the *spine* and the curve $y^2 + (z - d)^2 = 2^{2/3}$ denotes the *separatrix fan surface*. Arrows indicate the magnetic field direction. We identify this type of null point as a negative null (as defined by Parnell et al. 1996), since the fan surface consists of field lines approaching the null and the field lines forming the spine are directed away from the 3D null.

The equilibrium magnetic field is rotationally symmetric about $z = 0$ and this can be seen in Fig. 2, which shows a 3D representation of the magnetic skeleton. Here, the red lines denote the separatrix fan surface, as in Fig. 1, but the spine is now denoted in blue for clarity. The lower boundary, $z = 0$, shows the value of $B_z(x, y, 0)$ i.e. the line-of-sight magnetogram. Our isolated 3D null point is generated by a parasitic polarity (black) within a uniform magnetic field (grey) and thus the dashed green line indicates the location of the polarity inversion line (the radius of which is 0.27472). Mathematically, the

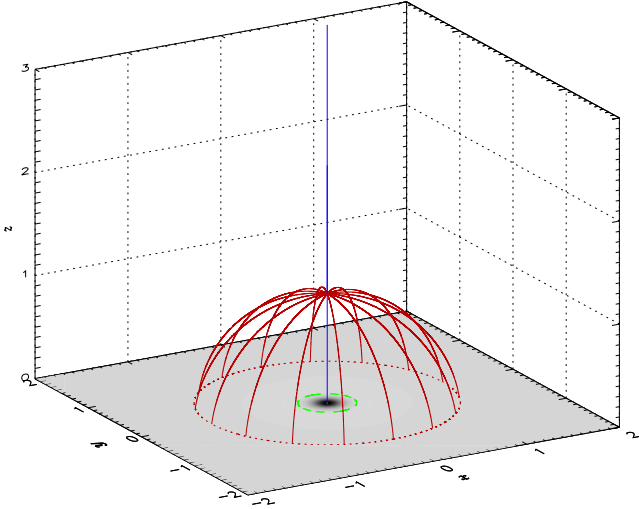


Figure 2. 3D representation of the magnetic skeleton. Here, the blue line denotes the spine, and the solid red lines denote the separatrix fan surface, described by $x^2 + y^2 + (z - d)^2 = R^2 = 2^{2/3}$, where $R = 2^{1/3}$. The lower boundary shows the value of $B_z(x, y, 0)$, i.e. the line-of-sight magnetogram. The dotted red circle indicates the (circular) footprint of the separatrix fan surface, described by radius $= \sqrt{R^2 - d^2} = \sqrt{2^{2/3} - 0.04} = 1.24395$. The dashed green line indicates the location of the polarity inversion line (radius = 0.274 72).

separatrix surface is the surface of a sphere described by $x^2 + y^2 + (z - d)^2 = R^2 = 2^{2/3}$. Since we have placed the dipole at $z = d = -0.2$, this means the separatrix surface forms a spherical dome of height $z = R + d = 2^{1/3} - 0.2 = 1.05992$ and with a circular footprint of radius $\sqrt{R^2 - d^2} = \sqrt{2^{2/3} - 0.04} = 1.24395$. This is denoted by a dotted red circle on the lower boundary/line-of-sight magnetogram in Fig. 2, i.e. this is the ‘footprint’ of the dome. Note that although \mathbf{B}_0 is inhomogeneous, it is still potential ($\nabla \times \mathbf{B}_0 = 0$) and solenoidal ($\nabla \cdot \mathbf{B}_0 = 0$). Note that as we move away from the null point, $\mathbf{B}_0 \rightarrow (0, 0, 1)$, i.e. we recover the uniform field. This is a more physically-realistic topology than that investigated in McLaughlin et al. (2008).

Previous work (see review by McLaughlin, Hood & De Moortel 2011b) has highlighted that the equilibrium Alfvén-speed profile $-v_A(x, y, z) = |\mathbf{B}_0(x, y, z)|$ plays a key role in dictating the propagation of the fast wave. Fig. 3 shows a colour contour of $v_A(0, y, z) = |\mathbf{B}_0(0, y, z)|$ in the $x = 0, yz$ -plane. The red lines denote the magnetic skeleton in this plane (as per Fig. 1). The contour shows clearly that the Alfvén-speed profile changes substantially across the magnetic domain and we observe that there is a small island of low Alfvén speed around the null point at $(x, y, z) = (0, 0, 1.05992)$, and that this is zero at the null itself (as per the definition). In contrast, the Alfvén-speed profile reaches a maximum at $x = y = z = 0$, i.e. the closest point in our domain (where $z \geq 0$) to the location of the (buried) dipole.

3 WKB APPROXIMATION

In this paper, we will be looking for WKB solutions (see e.g. Bender & Orszag 1978) of the form ,

$$\mathbf{v}_1(x, y, z, t) = \mathcal{V} e^{i\phi(x, y, z, t)}, \quad (9)$$

where \mathcal{V} is a constant vector matching the dimensions of the system. We define $\omega = \partial\phi/\partial t$ as the angular frequency and $\mathbf{k} = \nabla\phi = (p, q,$

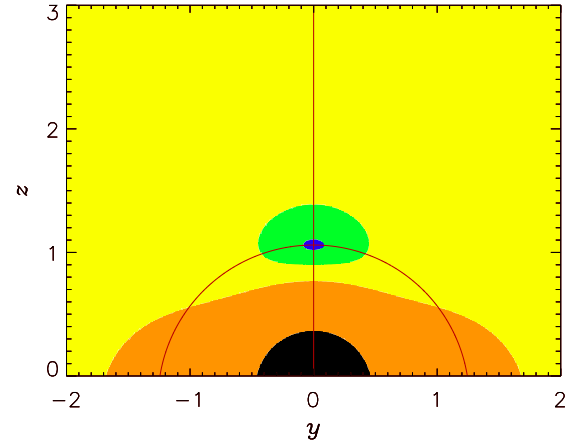


Figure 3. Equilibrium Alfvén-speed profile: colour contour of $v_A(0, y, z) = |\mathbf{B}_0(0, y, z)|$ in the $x = 0, yz$ -plane. Contour is colour coded: $0 \leq v_A \leq 0.1$ (blue); $0.1 \leq v_A \leq 0.5$ (green); $0.5 \leq v_A \leq 1.2$ (yellow); $1.2 \leq v_A \leq 10$ (orange); $v_A \geq 10$ (black). Red lines indicate the magnetic skeleton in this plane, which is rotationally-symmetric about the z -axis.

r) as the wavevector. For the WKB approach to be applicable, we consider ϕ and its derivatives to be large parameters in our system.

In order to isolate one of the different MHD wave modes (i.e. distinguishing between the fast and slow magnetoacoustic waves and the Alfvén wave), we now introduce a new set of coordinates $(\mathbf{B}_0, \mathbf{k}, \mathbf{B}_0 \times \mathbf{k})$. This coordinate system describes all three directions in space when $\mathbf{B} \not\propto \mathbf{k}$, i.e. $\mathbf{B}_0 \neq \alpha \mathbf{k}$, where α is an arbitrary constant of proportionality. This paper is interested primarily in the behaviour of the fast wave, which can propagate across magnetic field lines, and hence such a coordinate system is well suited to isolating the fast wave behaviour. Note that the work here is also valid for $\mathbf{B}_0 = \alpha \mathbf{k}$, but the consequence of which is that the solution is degenerate and one cannot distinguish between the fast wave and Alfvén wave (see Appendix A of McLaughlin et al. 2008, for full derivation).

The WKB approximation (equation 9) is substituted into equation (7) and we make the WKB approximation such that $\phi \gg 1$. Taking the scalar product with the coordinate system described above yields

$$\begin{bmatrix} \omega^2 & 0 & 0 \\ \mathbf{B}_0 \cdot \mathbf{k} |\mathbf{k}|^2 & \omega^2 - |\mathbf{B}_0|^2 |\mathbf{k}|^2 & 0 \\ 0 & 0 & \omega^2 - (\mathbf{B}_0 \cdot \mathbf{k})^2 \end{bmatrix} \cdot \begin{pmatrix} \mathbf{v}_1 \cdot \mathbf{B}_0 \\ \mathbf{v}_1 \cdot \mathbf{k} \\ \mathbf{v}_1 \cdot \mathbf{B}_0 \times \mathbf{k} \end{pmatrix} = \begin{pmatrix} 0 \\ 0 \\ 0 \end{pmatrix}$$

In order to avoid a trivial solution, the determinant of this matrix must be zero. Hence

$$\omega^2(\omega^2 - |\mathbf{B}_0|^2 |\mathbf{k}|^2)[\omega^2 - (\mathbf{B}_0 \cdot \mathbf{k})^2] = 0, \quad (10)$$

which has two solutions: corresponding to the fast magnetoacoustic mode and the Alfvén mode. The slow magnetoacoustic wave solution is absent under the cold plasma approximation.

3.1 WKB solution corresponding to fast magnetoacoustic wave

The fast magnetoacoustic wave is isolated in equation (10) by making the assumption $\omega^2 \neq (\mathbf{B}_0 \cdot \mathbf{k})^2$. Therefore, equation (10) simplifies to

$$\frac{1}{2} [\omega^2 - (B_x^2 + B_y^2 + B_z^2)(p^2 + q^2 + r^2)] = 0$$

$$= \mathcal{F}(\phi, \omega, t, \mathbf{B}_0, \mathbf{k}), \quad (11)$$

where \mathbf{B}_0 and \mathbf{k} have been expanded into component form, and $1/2$ has been introduced for convenience later on. Here, \mathcal{F} is a first-order, non-linear partial differential equation, which we solve using Charpit's Method (a variation on the method of characteristics, see e.g. Evans, Blackledge & Yardley 1999). Charpit's Method requires that all variables depend upon an independent variable in characteristic space, which we take as s . Hence, for this system the relevant Charpit's Equations are

$$\frac{d\phi}{ds} = \left(\omega \frac{\partial}{\partial \omega} + \mathbf{k} \cdot \frac{\partial}{\partial \mathbf{k}} \right) \mathcal{F}, \quad \frac{d\omega}{ds} = - \left(\frac{\partial}{\partial t} + \omega \frac{\partial}{\partial \phi} \right) \mathcal{F},$$

$$\frac{d\mathbf{k}}{ds} = - \left(\frac{\partial}{\partial \mathbf{r}} + \mathbf{k} \frac{\partial}{\partial \phi} \right) \mathcal{F}, \quad \frac{dt}{ds} = \frac{\partial \mathcal{F}}{\partial \omega}, \quad \frac{d\mathbf{r}}{ds} = \frac{\partial \mathcal{F}}{\partial \mathbf{k}},$$

recalling $\mathbf{k} = \nabla\phi = (p, q, r)$ and $\mathbf{r} = (x, y, z)$. This reduces the first-order partial differential equation in equation (11) to a set of ordinary differential equations, which are dependent upon only their initial conditions and evolution s along the characteristic curve. The relevant initial conditions for the variables are $\phi_0 = \phi(s=0)$, $\omega_0 = \omega(s=0)$, $t_0 = t(s=0)$, $x_0 = x(s=0)$, $y_0 = y(s=0)$, $z_0 = z(s=0)$, $p_0 = p(s=0)$, $q_0 = q(s=0)$, and $r_0 = r(s=0)$. The equations are progressed numerically from their initial positions and along their characteristic curve using a fourth-order Runge–Kutta method. It is worth noting there are no boundary conditions in the traditional sense: the variables are solved using Charpit's Method and the solutions depend only upon the initial position (x_0, y_0, z_0, t_0) and the extent s travelled along the characteristic curve. Hence, no boundary conditions are imposed and only initial conditions are required: this is a strength of the WKB approach, whereas for traditional numerical simulations the choice of boundary conditions can play a significant role.

Applying Charpit's Method to equation (11) yields

$$\frac{d\phi}{ds} = 0, \quad \frac{d\omega}{ds} = 0, \quad \frac{dt}{ds} = \omega,$$

$$\frac{dx}{ds} = -p|\mathbf{B}_0|^2, \quad \frac{dp}{ds} = \left(B_x \frac{\partial B_x}{\partial x} + B_y \frac{\partial B_y}{\partial x} + B_z \frac{\partial B_z}{\partial x} \right) |\mathbf{k}|^2,$$

$$\frac{dy}{ds} = -q|\mathbf{B}_0|^2, \quad \frac{dq}{ds} = \left(B_x \frac{\partial B_x}{\partial y} + B_y \frac{\partial B_y}{\partial y} + B_z \frac{\partial B_z}{\partial y} \right) |\mathbf{k}|^2,$$

$$\frac{dz}{ds} = -r|\mathbf{B}_0|^2,$$

$$\frac{dr}{ds} = \left(B_x \frac{\partial B_x}{\partial z} + B_y \frac{\partial B_y}{\partial z} + B_z \frac{\partial B_z}{\partial z} \right) |\mathbf{k}|^2, \quad (12)$$

where $|\mathbf{B}_0|^2 = B_x^2 + B_y^2 + B_z^2$ and $|\mathbf{k}|^2 = p^2 + q^2 + r^2$. All variables in the system are now dependent only on s and their initial position. Equation (12) yields some simplifications: $\phi(x, y, z, t) = \phi_0$, $\omega = \omega_0$ and $t = \omega_0 s + t_0$, where ϕ_0 , ω_0 and t_0 are constants.

The following initial conditions are now selected for equation (12),

$$\omega_0 = 2\pi, \quad t_0 = 0, \quad -3 \leq x_0 \leq 3, \quad -3 \leq y_0 \leq 3, \quad z_0 = 0,$$

$$p_0 = 0, \quad q_0 = 0, \quad r_0 = -\frac{\omega_0}{|\mathbf{B}_0(x_0, y_0, z_0)|}, \quad (13)$$

where this set of initial conditions corresponds to a fast magnetoacoustic wave being launched from $z = z_0 = 0$ and that is initially planar in the xy -plane.

Note that the equilibrium magnetic field in equation (8) is rotationally symmetric about $z = 0$ and so if equation (12) were to be presented in cylindrical polar coordinates, say (ζ, θ, z) under which $\mathbf{k} = \nabla\phi = (\frac{\partial\phi}{\partial\zeta}, \frac{1}{\zeta} \frac{\partial\phi}{\partial\theta}, \frac{\partial\phi}{\partial z}) = (k_\zeta, k_\theta, k_z)$ then

$$\frac{dk_\theta}{ds} = \mathbf{B}_0 \cdot \frac{1}{\zeta} \frac{\partial \mathbf{B}_0}{\partial \theta} |\mathbf{k}|^2 = 0, \quad (14)$$

since $\partial \mathbf{B}_0 / \partial \theta = 0$. Furthermore, in cylindrical polar coordinates, initial conditions (13) would be equivalent to $k_\theta = 0$ at $t = 0$ and so, by equation (14), $k_\theta = 0$ for all time. Hence

$$\frac{d\mathbf{r}}{ds} = \frac{\partial \mathcal{F}}{\partial \mathbf{k}} \Rightarrow \frac{\zeta d\theta}{ds} = \frac{\partial \mathcal{F}}{\partial k_\theta} = -k_\theta |\mathbf{B}_0|^2$$

$$\Rightarrow \frac{d\theta}{ds} = -\frac{1}{\zeta} k_\theta |\mathbf{B}_0|^2 = 0. \quad (15)$$

Given that $d\theta/ds = 0$, we predict the ray paths will lie on planes of constant θ . Note that the confinement of ray paths to planes of constant θ results from not only the rotationally-symmetric equilibrium magnetic field but also from our choice of initial conditions, specifically $k_\theta(t=0) = 0$.

4 FAST WAVE PROPAGATION

We now look at the propagation of the fast wave in the neighbourhood of our isolated null point and separatrix fan surface. The WKB approach considers individual elements that are generated at specific starting points and then gives their 3D position as the element progresses along their individual characteristic curve. This heralds two complementary avenues to analysing the wave evolution: we can follow and visualize the ray paths (or characteristic paths) of individual wave elements (Section 4.1) or we can construct surfaces of individual elements at specific times which are equivalent to the propagation of the wavefront (Section 4.2).

4.1 Ray paths

Figs 4 and 5 plot the ray paths of individual elements from an initially-planar wave generated along the xy -plane at $z = 0$. Our system is rotationally symmetric, so it is sufficient to present the results in the $x = 0, yz$ -plane. Fig. 4 shows the ray paths for starting points of $-2 \leq y_0 \leq -0.05$ to illustrate the propagation in the system. We have chosen specific starting points to best illustrate the overall behaviour: ray paths are plotted at intervals of 0.05 for $-2 \leq y_0 \leq -0.2$, then at intervals of 0.01 for $-0.2 \leq y_0 \leq -0.1$, and then specific ray paths generated from $y_0 = -0.09$ (yellow), $y_0 = -0.08$ (blue), $y_0 = -0.07$ (orange), $y_0 = -0.06$ (red), and $y_0 = -0.05$ (green). A star at $x = y = 0, z = 2^{1/3} - 0.2 = 1.05992$ denotes the 3D null point.

We see that the different ray paths experience *refraction*, albeit by varying severities, where individual rays are refracted towards the null point, i.e. a region of lower Alfvén speed, and are refracted away from close to $x = y = z = 0$, i.e. a region of high Alfvén speed, close to the dipole location. This is in agreement with the Alfvén-speed profile in Fig. (3). We see that ray paths generated for $y_0 \leq -1.5$ do not appear to be influenced greatly by the system and simply propagate in the direction of increasing z . Ray paths generated for $-1.5 \leq y_0 \leq -0.1$ experience refraction away from the dipole locus – for some ray paths this manifests as the crossing

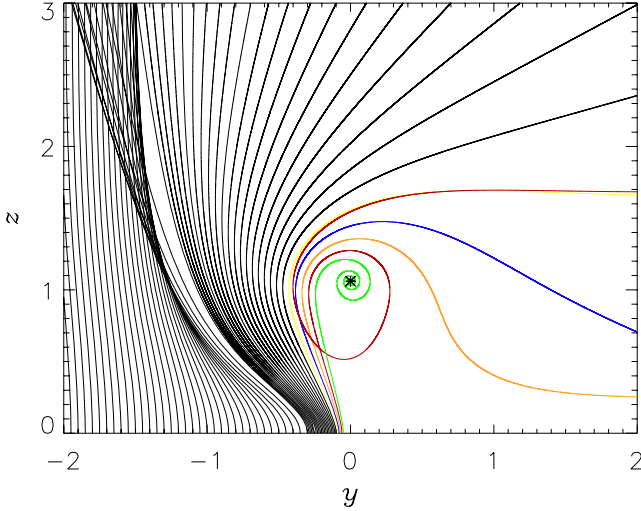


Figure 4. Ray paths for starting points of $x_0 = 0$, $-2 \leq y_0 \leq -0.05$, $z_0 = 0$ to demonstrate the general behaviour in the system. Individual characteristic curves are plotted at intervals of 0.05 for $-2 \leq y_0 \leq -0.2$, intervals of 0.01 for $-0.2 \leq y_0 \leq -0.1$, and then specific characteristics starting at $y_0 = -0.09$ (yellow), $y_0 = -0.08$ (blue), $y_0 = -0.07$ (orange), $y_0 = -0.06$ (red), and $y_0 = -0.05$ (green), respectively. A star denotes the location of the 3D null point at $x = y = 0$, $z = 2^{1/3} - 0.2 = 1.05992$.

over of ray paths in the top left corner of the subfigure – and for ray paths generated closer to the spine, they experience refraction towards the null – these ray paths propagate at varying angles to the z -direction. The individual ray paths for $y_0 = -0.09$ (yellow), $y_0 = -0.08$ (blue), and $y_0 = -0.07$ (orange) are influenced significantly by the topology, namely refracting towards the null but ultimately escaping towards the right of the subfigure. The ray path for the characteristic generated at $y_0 = -0.06$ (red) is first refracted towards the null point, then is refracted away from the dipole and is then refracted a second time around the null, before ultimately escaping the system. Finally, the ray path generated at $y_0 = -0.05$ (green) is captured fully by the null. It experiences refraction but ultimately does not escape the system; it spirals into the null point.

In Fig. 5a, the ray paths generated for $y_0 = -0.062$ (blue), $y_0 = -0.061$ (black), and $y_0 = -0.06$ (red) are shown. We present incremental steps of 0.001 to show that the final directions of the ray paths can vary substantially, and we can see that all three experience

refraction towards the null and varying levels of refraction away from the dipole locus. An extreme example of the sensitivity to the refraction phenomenon can be seen in the ray path generated for $y_0 = -0.053$ (Fig. 5b). Here, the characteristic undergoes multiple orbits around the null, before ultimately escaping. This is in contrast to Fig. 5c which shows the ray path generated for $y_0 = -0.0525$; here the characteristic spirals into the null and is ultimately captured by the null. We find that all ray paths generated on $x_0 = 0$, $-0.0525 \leq y_0 \leq 0.0525$, $z_0 = 0$ are captured by the null point and, due to the rotational symmetry, we identify this as the *critical radius* in our system, $r_{\text{critical}} = 0.0525$, where ray paths generated on $x_0, y_0, z_0 = 0$ are captured by the null if $x_0^2 + y_0^2 \leq r_{\text{critical}}^2$. Note that this is a critical radius on the $z = 0$ plane, not a spherical radius surrounding the null point. In this paper, we limit the spacing between initial points (our generated wave elements) to incremental steps of 0.0005.

4.2 Wavefront evolution

Let us now consider the wavefront propagation. Fig. 6 shows the location of the individual elements after a given time which can be understood as defining the location of the wavefront. Since $t = \omega_0 s + t_0$, each time corresponds to a particular value of s (recall s quantifies the evolution along an individual characteristic). An individual element is therefore described fully by its starting position (x_0, y_0, z_0) and its evolution along parameter s (note that z_0 is fixed here). Starting positions for $x_0 = 0$, $-3 \leq y_0 \leq 0$, $z_0 = 0$ are shown in Fig. 6, and each individual element is plotted as a cross (with an initially-uniform separation of 0.01) to elucidate the wave stretching. In each subfigure, the magnetic skeleton (red) in the yz -plane is shown for context.

We find that the fast wavefront starting between $-3 \leq y_0 \leq 0$ propagates in the direction of increasing z away from the lower boundary $z = 0$, but not all parts rise uniformly. The part of the wavefront (approximately $-0.45 \leq y \leq 0$) rises much faster than the rest, with the maximum occurring at $y = 0$. This is not due to the presence of the magnetic skeleton, but instead it is due to the inhomogeneous Alfvén-speed profile which deforms the wave from its original planar form and where each individual element (and therefore that part of the wavefront) propagates with its own local (Alfvén) speed. The behaviour is well understood from Fig. 3.

The subsequent evolution takes two different forms: First, the majority of the wavefront is deformed and deflected (dictated by the

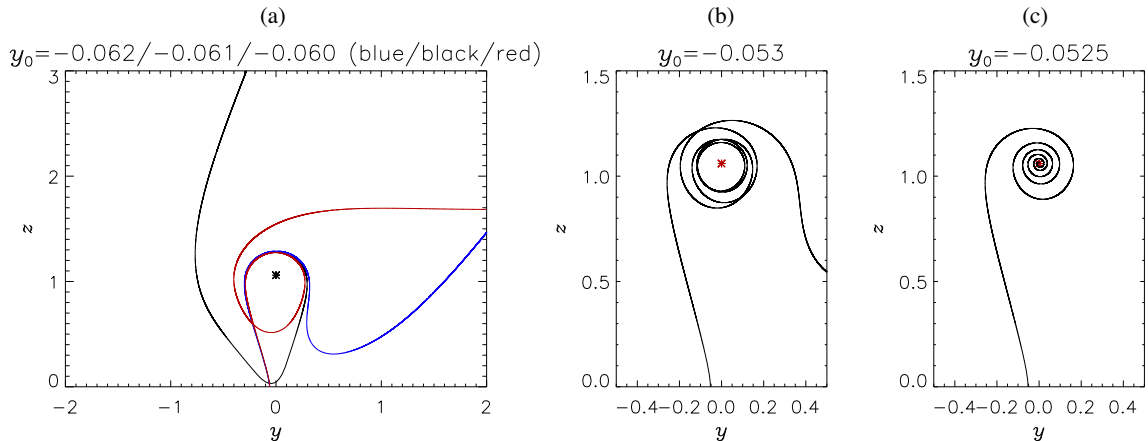


Figure 5. (a) Ray paths generated for $y_0 = -0.062$ (blue), $y_0 = -0.061$ (black), $y_0 = -0.06$ (red). (b) Ray paths from $y_0 = -0.053$. (c) Ray paths from $y_0 = -0.0525$.

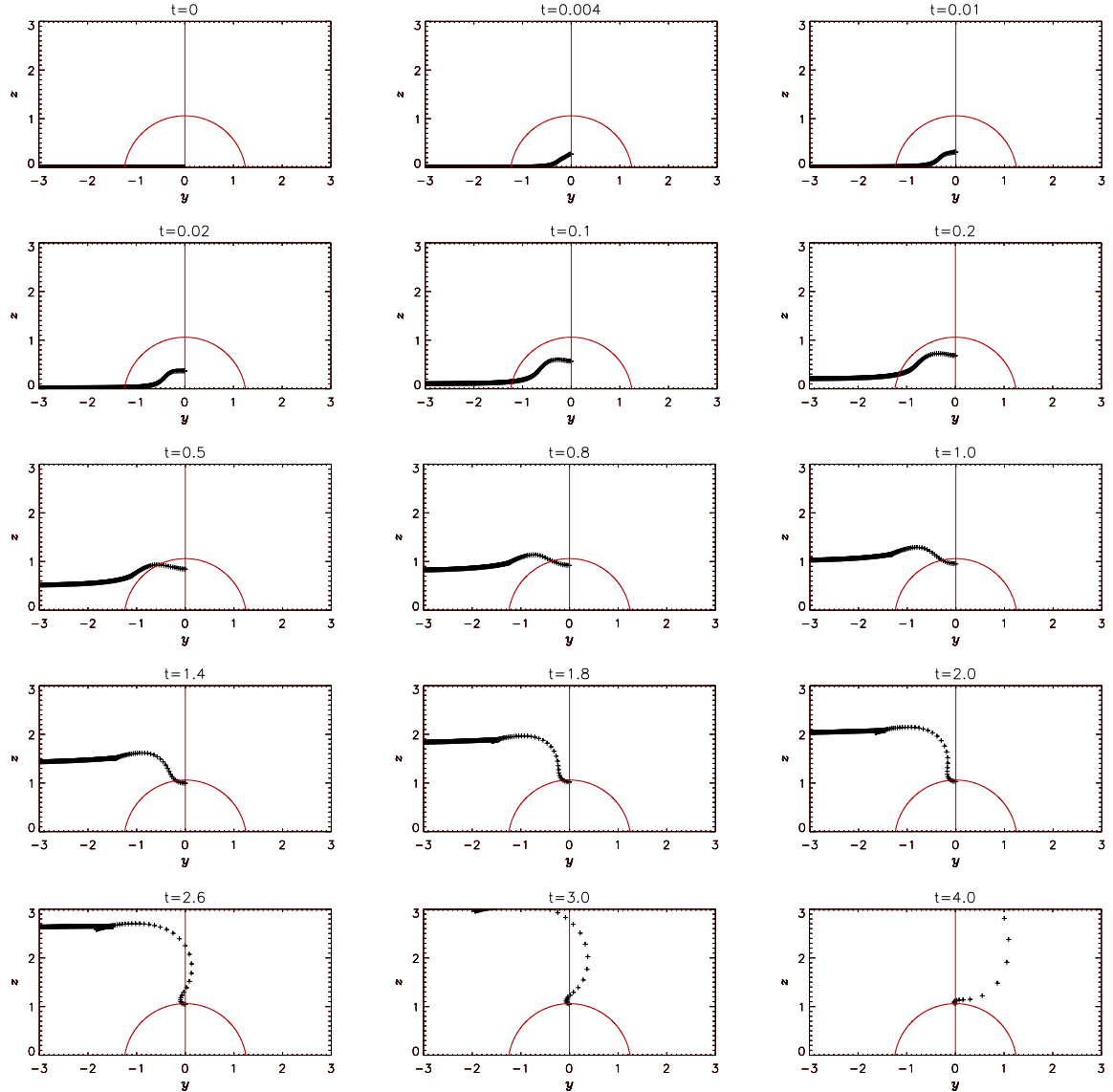


Figure 6. Location of ray paths at various times for WKB approximation of a fast wave generated on boundary $x_0 = 0$, for $-3 \leq y_0 \leq 0$, $z_0 = 0$ and its resultant propagation in the $x = 0$, yz -plane. Displayed times are chosen to best illustrate evolution and so time between frames is not uniform. The wavefront consists of crosses from the WKB solution, so as to illustrate clearly the evolution. The magnetic skeleton (red) in the yz -plane is shown for context.

varying equilibrium Alfvén-speed profile) but ultimately escapes the region and, secondly, a portion of the wave is trapped by the null point, in agreement with the results in Section 4.1. With two fates (escape or capture), the wavefront is stretched between its two ultimate destinations and this stretching manifests as an increase in the spacing between the crosses.

4.3 3D wave propagation

We can use the WKB solution to plot the 3D ray paths of individual elements generated at $(x_0, y_0, z_0 = 0)$. Fig. 7 shows the ray paths for individual elements that start along $z_0 = 0$ and are generated along the lines $y_0 = -x_0$ (Fig. 7a) and $y_0 = x_0$ (Fig. 7b), respectively. The ray paths denoted in green are those generated for $y_0 = \pm 0.0525$, i.e. the critical radius of capture, r_{critical} . For context, the magnetic skeleton (red) is shown in the plane of generation. As in Section 4.1, we see there are two types of behaviour: Characteristic curves

can be trapped by the null for $|x_0| \leq 0.0525$ or else escape the null, where the closer a ray path gets to the null or dipole, the stronger its deflection by the local Alfvén-speed profile. Fig. 7b also confirms the ray paths are confined to the azimuthal plane they are generated in, as predicted from equation (15).

We can also consider the propagation of an entire wavefront (the 3D equivalent of Section 4.2) but, given the ray paths are rotationally symmetric, there is little extra information to be gained. An example of a wavefront surface can be found in Appendix B.

5 PERCENTAGE OF WAVE CAPTURED

5.1 Radius and area of capture

From Section 4.1, we see that there are two types of behaviour: ray paths can be trapped (by refraction) at the null or else ultimately escape the null. This allows us to calculate a percentage of the wave

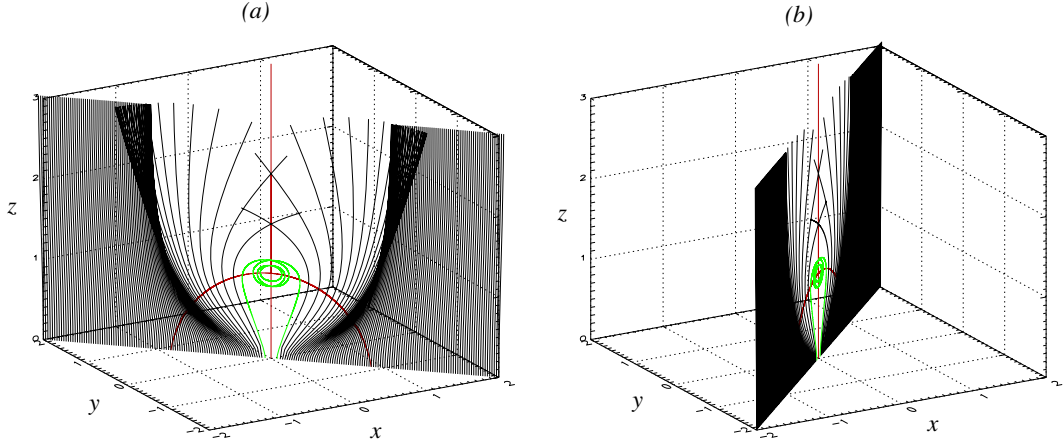


Figure 7. 3D ray paths for individual elements generated along $z_0 = 0$ and (a) $y_0 = -x_0$ and (b) $y_0 = x_0$. Green denotes ray path generated for $x_0 = \pm 0.0525$, i.e. captured. The magnetic skeleton (red) in the plane of generation is shown for context.

that is captured by the null. The radius of capture, which was found to be $r_{\text{critical}} = 0.0525$, is fixed for the system considered here, but to calculate a capture percentage we must make a choice for our initial input area. Note that in this paper we have presented results for initial conditions $-3 \leq x_0 \leq 3$, $-3 \leq y_0 \leq 3$ and $z_0 = 0$ (see equation 13) but since the WKB solution does not involve boundary conditions (only initial conditions) we would have obtained the same r_{critical} for any choice of initial area with $|(x_0, y_0, 0)| \geq r_{\text{critical}}$. Thus, we are free to choose the initial input area covered by the wavefront, but will always have a fixed r_{critical} and therefore (due to rotational symmetry) a fixed area of capture: $\pi(r_{\text{critical}})^2$.

In this paper, we choose to define the initial input area as the area underneath the dome, i.e. the area defined by the footprint of the dome at radius $\sqrt{R^2 - d^2} = \sqrt{2^{2/3} - 0.04} = 1.24395$ (see Fig. 2 for a visualization of the dome footprint). Under this definition, the (non-dimensionalized) area covered by the initially-planar wavefront is $\pi(R^2 - d^2) = 4.86130$ and the area of capture is $\pi(r_{\text{critical}})^2 = 0.0086590$. Thus, the percentage of the wave captured by the null point is 0.178 per cent.

5.2 Percentage of wave captured varying with null height

The magnetic topology considered so far in this paper (Section 2.2) can be generalized by the introduction of two dimensionless coefficients into equation (8). These coefficients, say \mathcal{A} and \mathcal{B} , can be used to alter the relative strengths of the magnetic dipole and uniform global field, respectively. A full generalization of the magnetic topology can be found in Appendix A, which shows that changing the coefficients can be used to alter the height of the magnetic null point, whilst preserving the dome topology.

Generalizing the magnetic topology gives us the opportunity to investigate how the radius of capture varies with null height. In order to adjust the null height here, we approach this by varying \mathcal{A} but keeping \mathcal{B} and d fixed ($\mathcal{B} = 1$, $d = -0.2$). Physically, for $\mathcal{A} > 1$ this is equivalent to considering a stronger, buried dipole that has the effect of ‘pushing’ the location of the null upwards. This varies the null height as governed by equation (A2), i.e. $z_{\text{null height}} = (2\mathcal{A})^{1/3} - 0.2$. We repeat the analytical work of Section 3 but now utilizing equation (A1) for our equilibrium magnetic field (note that initial conditions 13 are still valid).

We find that for each individual null height considered, we always find a single radius of capture (critical radius) for a given \mathcal{A} . This can be seen in Fig. 8a. We find that the critical radius decreases with null height, tending to a constant value of $r_{\text{critical}} = 0.0470$. In this paper, we limit the spacing of our initial points to incremental steps of 0.0005: recall the difference in behaviour between Fig. 5b (the ray path generated for $y_0 = -0.053$ escapes the null) and Fig. 5c (the ray path generated for $y_0 = -0.0525$ is captured by the null). Thus, we indicate error bars of ± 0.0005 in Fig. 8a. This spatial sensitivity was checked to be adequate for the most challenging cases investigated.

We then repeat the calculation of Section 5.1, i.e. we define the initial input area as the area defined by the footprint of the separatrix dome at radius $\sqrt{(\frac{2\mathcal{A}}{\mathcal{B}})^{2/3} - d^2}$. Each individual topology considered (varying \mathcal{A} , $\mathcal{B} = 1$, $d = -0.2$) then has its own radius of capture, say $r_{\text{critical}, \mathcal{A}}$, and the corresponding area of capture is always

$$\frac{(r_{\text{critical}, \mathcal{A}})^2}{\left(\frac{2\mathcal{A}}{\mathcal{B}}\right)^{2/3} - d^2} = \frac{(r_{\text{critical}, \mathcal{A}})^2}{(2\mathcal{A})^{2/3} - 0.04}.$$

This can be seen in Fig. 8b. We find that the percentage of the area under the dome captured decreases with null height.

6 CONCLUSION

We have investigated the behaviour of the fast magnetoacoustic wave within a separatrix dome magnetic topology that contains a 3D null point (the fan plane forms the dome). We consider the linearized MHD equations for an inhomogeneous, ideal, cold ($\beta = 0$) plasma. The equations are solved utilizing the WKB approximation, followed by Charpit’s Method. The WKB approach allowed us two complementary avenues to analysing the wave evolution: We can follow the ray paths of individual wave elements and can also consider the location of the wavefront at specific times (equivalent to the propagation of the wavefront).

We find that for a planar fast wave generated below the null point, the propagation is strongly dependent on its initial location and there are two main behaviours: the majority of the wave escapes the null (experiencing different severities of refraction depending on specific location) and part of the wave is captured by the 3D

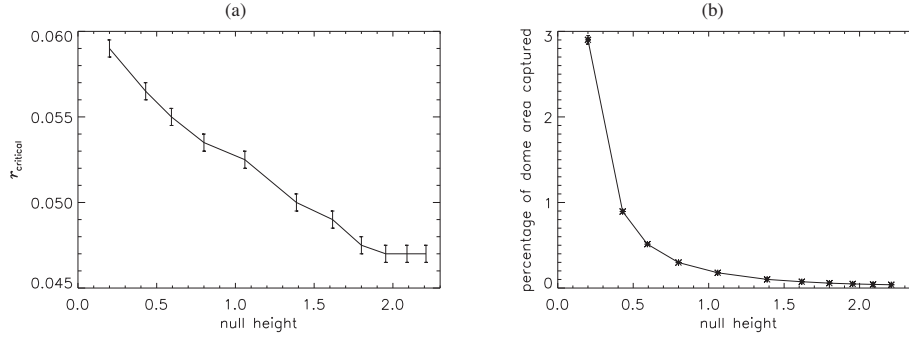


Figure 8. Parametric study of how (a) radius of capture (r_{critical}) varies with null height, and (b) percentage of area-under-the-dome captured versus null height. Error bars of ± 0.0005 are included.

null. We find that there exists a critical radius in the initial $z = 0$ plane (there is rotational symmetry about the spine, i.e. the z -axis), which we call a radius of capture, r_{critical} , which separates the two types of behaviour, such that a wave element generated at $(x_0, y_0, 0)$ is captured by the null provided $x_0^2 + y_0^2 \leq r_{\text{critical}}^2$. We also find that the ray paths are confined to the azimuthal plane that they are generated in, provided they are initialized with no azimuthal component (as per our initial condition).

Section 4.2 demonstrated that, given the two fates (escape or capture), the wavefront is stretched between its two ultimate destinations; this stretching is visualized in Fig. 6 as an increase in the spacing between the crosses. Note that under the WKB approach, this (extreme) stretching can manifest, but the wave ‘front’ can never truly split – the surface is constructed from individual ray paths (individual crosses) which are independent of each other and so there is nothing to split. It is expected that in reality stretching will eventually lead to steep gradients facilitating a genuine splitting of the front due to enhanced visco-resistive dissipation (essentially, this is ‘phase mixing’ due to the field inhomogeneity around the null, see e.g. Heyvaerts & Priest 1982; Nakariakov et al. 1997; Botha et al. 2000; McLaughlin et al. 2011a). However, the WKB approach as presented here does not capture such physics.

We also present a generalization of the magnetic topology in Appendix A by introducing dimensionless coefficients \mathcal{A} and \mathcal{B} , which are used to alter the relative strengths of the magnetic dipole and uniform global field, respectively. We find that mathematically the separatrix surface will always be the surface of a sphere described by $x^2 + y^2 + (z - d)^2 = (\frac{2\mathcal{A}}{\mathcal{B}})^{2/3}$, corresponding to a null height of $(\frac{2\mathcal{A}}{\mathcal{B}})^{1/3} + d$, and with a circular footprint of radius $\sqrt{(\frac{2\mathcal{A}}{\mathcal{B}})^{2/3} - d^2}$ (valid for $d \leq 0$). Thus, changing coefficients \mathcal{A} and \mathcal{B} can be used to alter the height of the magnetic null point, whilst – crucially – preserving the dome topology. We note that the magnetic field considered in Section 2.2 can be recovered by setting $\mathcal{A} = \mathcal{B} = 1$. The height of the null can also be controlled by modifying d .

For the magnetic topology described in Section 2.2, we find $r_{\text{critical}} = 0.0525$. In this paper, we limit the spacing of our initial condition to incremental steps of 0.0005, but the resolution of our Runge–Kutta approach could be improved to consider smaller incremental steps if required. Utilizing our generalization of the magnetic topology, we also conducted a parametric study of how r_{critical} varies with null height. We find that the value of the critical radius decreases as the height of the null increases. We also find that the critical radius (as a function of null height) tends towards a constant value of 0.0470.

We also calculated the percentage of the wave that is captured by the null. We find that r_{critical} is fixed once the specific topology for the system is chosen, but that we have a free choice to define what we consider as the initial input. In this paper, we chose the initial input to be the area defined by the footprint of the dome on our model photosphere ($z = 0$). Under this definition, the percentage of the wave captured by the null point considered in Section 2.2 is 0.178 per cent. We also utilized our parametric study to find that the percentage captured of the area under the dome decreases with null height, and that, for the parameters considered, the percentage is never greater than 3 per cent.

We have limited our investigation to understanding the fast wave in the cold plasma limit, but we could have also investigated the second root of equation (10) by assuming $\omega^2 \neq |\mathbf{B}_0|^2 |\mathbf{k}|^2$. This would yield the equations governing the Alfvén wave behaviour.

It is also possible to extend the work in this paper by dropping the cold plasma assumption, which will lead to a third root of equation (10) which will correspond to the behaviour of the slow magnetoacoustic wave, and also allow for acoustic contributions to the fast speed (i.e. $v_{\text{fast}}^2 = v_A^2 + c_s^2$ is possible), where c_s is the sound speed, with fast waves taking on a predominantly-acoustic character in the very close vicinity of the null (as $\mathbf{B}_0 \rightarrow 0$). This will modify equation (7) such that

$$\frac{\partial^2 \mathbf{v}_1}{\partial t^2} = c_s^2 \nabla (\nabla \cdot \mathbf{v}_1) + \{\nabla \times [\nabla \times (\mathbf{v}_1 \times \mathbf{B}_0)]\} \times \mathbf{B}_0. \quad (16)$$

Equation (16) is derived in the same way as equation (7), but without making the assumption of a cold plasma. A full investigation of equation (16) is outside the scope of this paper, but we do note that both equations (16) and (7) are valid for any suitable choice of equilibrium magnetic field, \mathbf{B}_0 . In other words, the 3D WKB technique described in this paper can be both applied to other magnetic configurations and extended further (e.g. by dropping the cold plasma assumption), although there are also limitations of such approaches – see the conclusions of McLaughlin et al. (2016). For further information on the WKB method and the wider-family of ray tracing methods, see Tracey et al. (2014).

Our results show that it is the location of the null point (which denotes the *global minimum* of our equilibrium Alfvén-speed profile) as well as distance relative to $x = y = z = 0$ (the point in our domain closest to the location of the buried dipole, corresponding to the *global maximum*) that play key roles in the fast wave propagation. Conversely, we find that the separatrix surface itself does not play a role, and the separatrix fan surface does not align with any key features in the equilibrium Alfvén-speed profile.

Previous work highlighted that the equilibrium Alfvén-speed profile plays a key role in dictating the propagation of the fast wave (e.g. see McLaughlin et al. 2011b), and we conclude that our results support this idea. Note that within the cold-plasma conditions studied here the separatrix surfaces play no role, but it has been shown, e.g. by Tarr et al. (2017), that separatrix surfaces do play an important role in guiding slow magnetoacoustic waves, and that these can be generated from fast-mode waves via mode conversion around the null for a $\beta \neq 0$ plasma (see McLaughlin & Hood 2006b and Tarr et al. 2017 for discussions of mode coupling about null points). So if the model in this paper was extended beyond the cold-plasma assumption, mode conversion would be expected to occur and so separatrix surfaces could play an important role (for the generated slow waves).

In this paper, we find that the fast wave experiences a complex refraction effect and that this *refraction effect is a key feature of fast wave propagation within inhomogeneous media*. This refraction effect causes upwardly-propagating waves originating from below the null point to be attracted to and trapped in the close vicinity of the null, provided the wave-packet originates sufficiently close to the spine field line (the requirements for which we have quantified). Such waves in our model are physically representative of, say, upwardly-propagating fast-mode waves transmitted from the top of the transition region. Thus, the energy associated with such waves will collect preferentially on small scales near the null, where a number of physical processes may occur to subsequently dissipate or convert the energy to other forms, namely localized current sheet formation, the triggering of magnetic reconnection, and enhanced visco-resistive dissipation of energy brought into the null by the waves (see Thurgood et al. 2017, 2018a,b for details of such physics close to the null). The findings presented in this paper, in a physically-representative null-point-containing field, that wave energy does indeed collect near null points also justifies independently the often a priori initial conditions of models which consider the specific details of subsequent phenomena occurring close to the null (due to non-linear and non-ideal processes, such studies often involve full MHD simulation of a small domain close to the null, with the assumption that some externally-originating wave has impinged upon the immediate neighbourhood of the null point as a necessary simplification).

Thus, we deduce that 3D coronal null points whose fan field lines form a dome – a common feature in the solar corona as revealed in potential field extrapolations – will be preferential locations of fast wave energy collection and deposition, where associated magnetic reconnection and visco-resistive heating can then occur. We find that only a small percentage of initial wave energy will be captured by the null, but in spite of this, the strong refraction effect will still focus that wave energy into a specific location of the magnetic topology and it is at this area where preferential heating will occur.

ACKNOWLEDGEMENTS

JAM and JOT acknowledge generous support from the Leverhulme Trust and this work was funded by a Leverhulme Trust Research Project Grant: RPG-2015-075. JAM and GJJ were also supported by STFC grant ST/L006243/1. All the authors acknowledge IDL support provided by STFC.

REFERENCES

- Afanasyev A. N., Uralov A. M., 2011, *Sol. Phys.*, 273, 479
 Afanasyev A. N., Uralov A. M., 2012, *Sol. Phys.*, 280, 561

- Bender C. M., Orszag S. A., 1978, *Advanced Mathematical Methods for Scientists and Engineers*. McGraw-Hill, New York
 Botha G. J. J., Arber T. D., Nakariakov V. M., Keenan F. P., 2000, *A&A*, 363, 1186
 Candelaresi S., Pontin D. I., Hornig G., 2016, *ApJ*, 832, 150
 De Moortel I., 2005, *Phil. Trans. Roy. Soc. A*, 363, 2743
 Edwards S. J., Parnell C. E., 2015, *Sol. Phys.*, 290, 2055
 Evans G., Blackledge J., Yardley P., 1999, *Analytical Methods for Partial Differential Equations*. Springer-Verlag, London
 Finn J. M., 2006, *Nat. Phys.*, 2, 445
 Griffiths D. J., 2004, *Introduction to Quantum Mechanics*. Cambridge Univ. Press, Cambridge
 Heyvaerts J., Priest E. R., 1983, *A&A*, 117, 220
 Khomenko E., Collados M., 2006, *ApJ*, 653, 739
 Longcope D. W., 2005, *Living Rev. Solar Phys.*, 2, 7
 McLaughlin J. A., Hood A. W., 2004, *A&A*, 420, 1129
 McLaughlin J. A., Hood A. W., 2005, *A&A*, 435, 313
 McLaughlin J. A., Hood A. W., 2006a, *A&A*, 452, 603
 McLaughlin J. A., Hood A. W., 2006b, *A&A*, 459, 641
 McLaughlin J. A., Ferguson J. S. L., Hood A. W., 2008, *Sol. Phys.*, 251, 563
 McLaughlin J. A., De Moortel I., Hood A. W., Brady C. S., 2009, *A&A*, 493, 227
 McLaughlin J. A., De Moortel I., Hood A. W., 2011a, *A&A*, 527, A149
 McLaughlin J. A., Hood A. W., De Moortel I., 2011b, *Space Sci. Rev.*, 158, 205
 McLaughlin J. A., Botha G. J. J., Régnier S., Spoor D. L., 2016, *A&A*, 591, 16
 Nakariakov V. M., Verwichte E., 2005, *Liv. Rev. Sol. Phys.*, 2, 3
 Nakariakov V. M., Roberts B., Murawski K., 1997, *Sol. Phys.*, 175, 93
 Nakariakov V. M. et al., 2016, *Space Sci. Rev.*, 200, 75
 Núñez M., 2017, *Commun. Nonlinear Sci. Numer. Simul.*, 43, 158
 Núñez M., 2018, *Eur. J. Mech. B*, 68, 100
 Parnell C. E., Smith J. M., Neukirch T., Priest E. R., 1996, *Phys. Plasmas*, 3, 759
 Pontin D. I., Hornig G., Priest E. R., 2005, *Geophys. Astrophys. Fluid Dyn.*, 99, 77
 Pontin D. I., Priest E. R., Galsgaard K., 2013, *ApJ*, 774, 154
 Priest E. R., Forbes T. G., 2000, *Magnetic Reconnection: MHD Theory and Applications*. Cambridge Univ. Press, Cambridge
 Priest E., 2014, *Magnetohydrodynamics of the Sun*. Cambridge Univ. Press, Cambridge
 Priest E. R., Titov V. S., 1996, *Phil. Trans. Roy. Soc.*, 354, 2951
 Régnier S., Parnell C. E., Haynes A. L., 2008, *A&A*, 484, L47
 Régnier S., 2013, *Sol. Phys.*, 288, 481
 Roberts B., 2004, *SOHO 13: Waves, Oscillations and Small-Scale Transient Events in the Solar Atmosphere: a Joint View from SOHO and TRACE* ESA SP-547. ESA, Spain, p. 1
 Shadowitz A., 1975, *The Electromagnetic Field* Dover Publications Inc., Dover Publications Inc, England
 Tarr L. A., Linton M., Leake J., 2017, *ApJ*, 837, 94
 Thurgood J. O., McLaughlin J. A., 2012, *A&A*, 545, 11
 Thurgood J. O., McLaughlin J. A., 2013a, *A&A*, 555, 7
 Thurgood J. O., McLaughlin J. A., 2013b, *A&A*, 558, 10
 Thurgood J. O., Pontin D. I., McLaughlin J. A., 2017, *ApJ*, 844, 2
 Thurgood J. O., Pontin D. I., McLaughlin J. A., 2018a, *ApJ*, 855, 50
 Thurgood J. O., Pontin D. I., McLaughlin J. A., 2018b, *Phys. Plasmas*, 25, 072105
 Tracy E. R., Brizard A. J., Richardson A. S., Kaufman A. N., 2014, *Ray Tracing and Beyond: Phase Space Methods in Plasma Wave Theory*. Cambridge Univ. Press, Cambridge

APPENDIX A: GENERALISED MAGNETIC TOPOLOGY

The magnetic topology considered in Section 2.2 can be generalized by the introduction of two dimensionless coefficients into equation (8). These coefficients, say \mathcal{A} and \mathcal{B} , can be used to alter

the relative strengths of the magnetic dipole and uniform global field, respectively. This alters equation (8) giving

$$\begin{aligned} B_x &= -\mathcal{A} \left\{ \frac{3x(z-d)}{[x^2 + y^2 + (z-d)^2]^{5/2}} \right\}, \\ B_y &= -\mathcal{A} \left\{ \frac{3y(z-d)}{[x^2 + y^2 + (z-d)^2]^{5/2}} \right\}, \\ B_z &= \mathcal{A} \left\{ \frac{x^2 + y^2 - 2(z-d)^2}{[x^2 + y^2 + (z-d)^2]^{5/2}} \right\} + \mathcal{B}. \end{aligned} \quad (\text{A1})$$

Recall that the dipole is placed at $\mathbf{r}_0 = (0, 0, d)$, where $|d|$ is the depth below our model photosphere ($z = 0$).

The null height can be calculated using the following ratio of coefficients

$$z_{\text{null height}} = \left(\frac{2\mathcal{A}}{\mathcal{B}} \right)^{1/3} + d, \quad (\text{A2})$$

where this ratio is computed by setting $\mathbf{B}_0 = 0$ and due to the rotational symmetry must lie along $x = y = 0$.

The equilibrium vector potential is calculated via

$$\begin{aligned} \mathbf{A}_{\text{total}} &= \mathbf{A}_{\text{dipole}} + \mathbf{A}_{\text{uniform field}} \\ &= \mathcal{A} \left(\frac{y}{[x^2 + y^2 + (z-d)^2]^{3/2}}, -\frac{x}{[x^2 + y^2 + (z-d)^2]^{3/2}}, 0 \right) \\ &\quad + \mathcal{B} \left(-\frac{y}{2}, \frac{x}{2}, 0 \right). \end{aligned} \quad (\text{A3})$$

Note there is symmetry under $x \rightarrow -y$. Therefore, we may consider the $x = 0$, yz -plane for further insight. Considering $x = 0$, the $\hat{\mathbf{x}}$ -component of equation (A3) gives

$$\hat{\mathbf{x}} \cdot \mathbf{A}_{\text{total}} = \frac{\mathcal{A}y}{[y^2 + (z-d)^2]^{3/2}} - \frac{\mathcal{B}y}{2}.$$

The separatrix surface is found when this is equal to zero. One solution to this is $y = 0$; this is the *spine*. The solution where $y \neq 0$ yields

$$y^2 + (z-d)^2 = \left(\frac{2\mathcal{A}}{\mathcal{B}} \right)^{2/3}.$$

Hence, mathematically the separatrix surface will always be the surface of a sphere described by $x^2 + y^2 + (z-d)^2 = (\frac{2\mathcal{A}}{\mathcal{B}})^{2/3}$. This means the separatrix surface will always be a spherical dome of height $z_{\text{null height}} = (\frac{2\mathcal{A}}{\mathcal{B}})^{1/3} + d$, in agreement with equation (A2), and with a circular footprint of radius $\sqrt{(\frac{2\mathcal{A}}{\mathcal{B}})^{2/3} - d^2}$, valid for $d \leq 0$.

Thus, changing the coefficients \mathcal{A} and \mathcal{B} can be used to alter the height of the magnetic null point, whilst preserving the dome

topology. Note that the height of the null can also be controlled by modifying d . The magnetic field considered in Section 2.2 can be recovered by setting $\mathcal{A} = \mathcal{B} = 1$.

APPENDIX B: THREE-DIMENSIONAL WAVEFRONT SURFACES

We can also consider the propagation of an entire wavefront (the 3D equivalent of Section 4.2). Fig. B1 shows the location of the wavefront at $t = 0.5$, showing the behaviour of the initially-planar wavefront that was generated on $-2 \leq x_0 \leq 2$, $-2 \leq y_0 \leq 2$, $z_0 = 0$. The surface is presented as a mesh, with an initially-uniform point

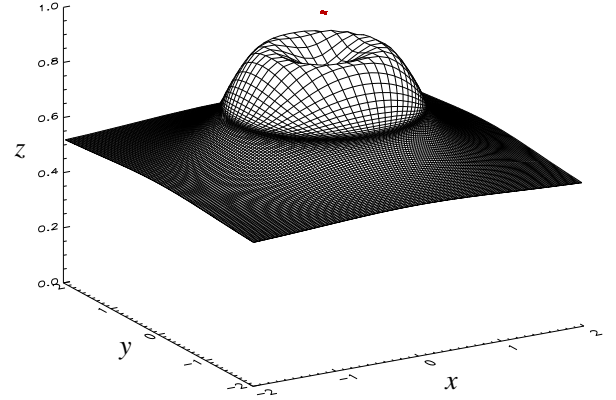


Figure B1. Location of the wavefront at $t = 0.5$ for initially-planar wavefront generated on $-2 \leq x_0 \leq 2$, $-2 \leq y_0 \leq 2$, $z_0 = 0$. The red block denotes the location of the null $(0, 0, 1.05992)$.

spacing.³ A red block denotes the location of the null $(0, 0, 1.05992)$. We see that the wavefront propagates in the direction of increasing z and that the wavefront is distorted (it is initially planar at $z_0 = 0$). The parts of the wavefront closest to the null are propagating at a lower speed than those around it, resulting in a local trough forming under the null. Again, the behaviour is entirely dictated by the inhomogeneous equilibrium Alfvén-speed profile.

Fig. B1 is the 3D companion of the $t = 0.5$ subfigure in Fig. 6. From the results in Section 4.2, we know that at later times the wavefront begins wrapping around the null and so the wavefront become distorted significantly, i.e. there is little extra information to be gained from looking at wavefront surfaces at later times. Hence, we only present a single wavefront surface in Fig. B1.

³For clarity of presentation in Fig. B1, we present a spacing of only 1 in every 10 points used to construct the surface.

This paper has been typeset from a \LaTeX file prepared by the author.